Author Manuscript

Author Manuscript

Author Manuscript

Author Manuscript

HHS Public Access

Author manuscript

ACS Nano. Author manuscript; available in PMC 2017 March 02.

Published in final edited form as:

ACS Nano. 2017 February 28; 11(2): 2227–2238. doi:10.1021/acsnano.6b08731.

Tumor-Penetrating Nanoparticles for Enhanced Anticancer Activity of Combined Photodynamic and Hypoxia-Activated Therapy

Yazhe Wang[†,‡], **Ying Xie**[†], **Jing Li**[†], **Zheng-Hong Peng**[†], **Yuri Sheinin**[§], **Jianping Zhou**[‡], and **David Oupický**[†,‡]

[†]Center for Drug Delivery and Nanomedicine, Department of Pharmaceutical Sciences, University of Nebraska Medical Center, Omaha, Nebraska, United States

[‡]Key Laboratory of Natural Medicines, Department of Pharmaceutics, China Pharmaceutical, University, Nanjing, Jiangsu, China

[§]Department of Pathology and Microbiology, University of Nebraska Medical Center, Omaha, Nebraska, United States

Abstract

Poor tumor penetration is a major challenge for the use of nanoparticles in anticancer therapy. Moreover, the inability to reach hypoxic tumor cells which are distant from blood vessels results in inadequate exposure to antitumor therapeutics and contributes to development of chemoresistance and increased metastasis. In the present study, we developed iRGD-modified nanoparticles for simultaneous tumor delivery of a photosensitizer indocyanine green (ICG) and hypoxia-activated prodrug tirapazamine (TPZ). The iRGD-modified nanoparticles loaded with ICG and TPZ showed significantly improved penetration in both 3D tumor spheroids *in vitro* and orthotopic breast tumors *in vivo*. ICG-mediated photodynamic therapy upon irradiation with a near-IR laser induced hypoxia, which activated antitumor activity of the co-delivered TPZ for synergistic cell-killing effect. *In vivo* studies demonstrated that the nanoparticles could efficiently deliver the drug combination in 4T1 orthotopic tumors. Primary tumor growth and metastasis were effectively inhibited by the iRGD-modified combination nanoparticles with minimal side effects. The results also showed the anticancer benefits of co-delivering ICG and TPZ in single nanoparticle formulation in contrast to a mixture of nanoparticles containing individual drugs. The study demonstrates the benefits of combining tumor-penetrating nanoparticles with hypoxia-activated drug treatment and establishes a delivery platform for PDT and hypoxia-activated chemotherapy.

Graphical abstract

Correspondence to: Jianping Zhou; David Oupický.

Supporting information. Additional nanoparticle characterization, cellular uptake and apoptosis analysis, and *in vivo* data are available in the supporting information.

Notes. The authors declare no competing financial interest.

Author Manuscript Author Manuscript Author Manuscript Author Manuscript

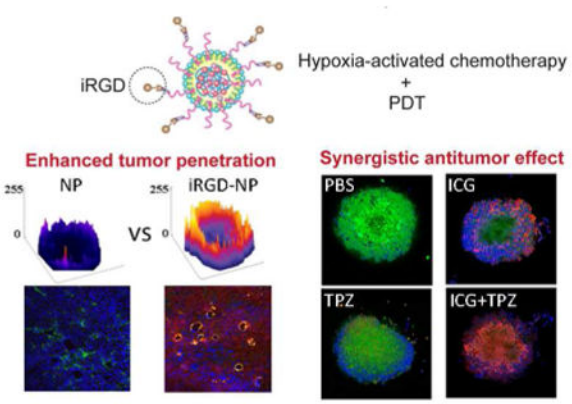

Keywords

Nanoparticles; Photodynamic Therapy; Hypoxia; Cancer; Tumor Penetration; iRGD

Tumor-targeted nanoparticle-based drug delivery systems have been widely explored in the development of novel anticancer treatment strategies.[1-3] Unfortunately, despite decades of intensive research, most of the targeted strategies failed to live up to clinical expectations.[4] Better understanding of tumor biology and factors that control transport and retention of nanoparticles in solid tumors enabled identification of the main causes of the poor performance of nanoparticles in tumor drug delivery.[5] Among the most important factors is the increased interstitial fluid pressure and the dense tumor stroma which both hinder transport of nanoparticles across more than one or two cell layers away from the blood vessels.[6-8] Such intratumoral diffusion resistance stands as intractable obstacle and significantly impairs the drug delivery efficacy and overall performance in cancer treatments. Moreover, the inability to reach hypoxic tumor cells which are distant from blood vessels results in inadequate exposure to antitumor therapeutics and contributes to development of chemoresistance and increased metastasis.[9] With this understanding, the design of effective drug delivery systems needs to take the intratumoral delivery aspects into consideration. Recently developed iRGD peptide can increase vascular and tissue permeability using a mechanism dependent on $\alpha\nu$ integrin and neuropilin-1. As a result, iRGD can function as both a tumor-homing and a tumor-penetrating peptide[10,11] and iRGD-modified nanoparticles may achieve enhanced drug accumulation in tumors through deep intratumoral penetration and targeted tumor distribution, ultimately benefiting the therapeutic performance of the nanoparticles.[12-14]

Photodynamic therapy (PDT) is an emerging treatment modality for various malignant and nonmalignant diseases.[15-18] PDT utilizes reactive oxygen species (ROS) generated through the reaction between a photosensitizer and oxygen present in tissues upon the irradiation with light to achieve effective treatment. However, hypoxia is a consequence of the oxygen consumption during PDT. Hypoxia is one of the factors responsible for the poor responses in PDT as well as in conventional radiotherapy and chemotherapy.[19-23] To overcome the negative consequences of PDT, multiple innovative strategies have been introduced, including oxygen codelivery and development of less oxygen-dependent PDT.[24-28] However,

Author Manuscript Author Manuscript Author Manuscript Author Manuscript

most of these strategies may encounter significant challenges in further clinical translation due to the heterogeneity of cancer and the involvement of multiple pathways in the pathogenesis, which are unlikely solvable by a monotherapy approach. Of note, hypoxia-directed treatment relies on oxygen-deficient environment for activating bioreductive prodrugs to potentiate the antitumor efficacy of PDT.[29,30] Several hypoxia-activated prodrugs, including banoxantrone, NLCQ-1 and dinitrobenzamide mustards, are in preclinical or early clinical development. Tirapazamine (TPZ) is another example of such prodrug, which exhibits high selective toxicity to hypoxic tumor cells in our pilot study. TPZ undergoes metabolism by reductases to generate transient oxidizing radical, which can be efficiently scavenged by molecular oxygen in normal tissues to re-form the parent compound.[31,32] However, in the absence of oxygen (as in hypoxia) the re-formation of the parent drug does not occur. Instead, the superoxide TPZ radical removes hydrogen from nearby macromolecules and causes structural damage.[33] Therefore, combining PDT and TPZ-mediated hypoxia-activated chemotherapy promises synergistic enhancement of cancer therapy.

In this study, we report development of hybrid PLGA/lipid nanoparticles capable of codelivering a photosensitizer indocyanine green (ICG) and hypoxia-activated prodrug TPZ (NP/IT) for improved antitumor therapeutic effect in metastatic breast cancer. ICG, a near-infrared (NIR) dye, is approved by the US FDA as a clinical diagnosis agent.[34] Due to its NIR optical features within optimal absorption window for biomedical applications, ICG has been intensively studied for PDT and NIR fluorescence imaging.[18,35,36] The developed nanoparticles are further conjugated with iRGD through copper-free click chemistry, providing nanoparticles (iNP/IT) with intratumoral penetration capability and improved antitumor performance. We hypothesized that after enhanced accumulation and penetration in solid tumors mediated by the iRGD-targeted nanoparticles, ICG would produce ROS in response to NIR laser irradiation and cause cell death under normal oxygen condition. In the meantime, the hypoxic microenvironment in tumors (in part created by PDT-induced oxygen depletion) triggers TPZ to enhance local cell killing, thus enhancing the overall anticancer effect (Scheme 1).

Results and Discussion

Preparation and characterization of nanoparticles

We have used a modified single-step nanoprecipitation method to prepare hybrid PLGA/lipid nanoparticles with co-encapsulated photosensitizer ICG and anticancer drug TPZ (NP/IT) (Table 1). The nanoparticles were prepared from a mixture of ICG, TPZ, PLGA, DPPC, DSPE-PEG and DSPE-PEG-DBCO. The core of the particles contained PLGA with co-encapsulated ICG and TPZ. The drug-PLGA core was coated with a lipid monolayer containing PEG chains for colloidal stabilization as reported previously.[37] In order to facilitate tumor targeting of the nanoparticles and to improve their penetration in solid tumors, we have conjugated iRGD onto the surface of the nanoparticles. The iRGD conjugation was accomplished using copper-free click chemistry between azide-terminated iRGD and cyclooctyne-containing DSPE-PEG-DBCO (Scheme 1). The content of the iRGD in the nanoparticles was determined as 7.3 wt% by amino acid analysis.

Author Manuscript Author Manuscript Author Manuscript Author Manuscript

To confirm the formation of the hybrid nanoparticles, the morphology of the iRGD-targeted nanoparticles containing ICG and TPZ (iNP/IT) was determined by TEM. The iNP/IT appeared as individual spherical particles with the expected core-shell structure and a size around 100 nm (Figure 1A). The particle size was then confirmed by DLS. The hydrodynamic diameter of iNP/IT was 112 nm with polydispersity index of 0.15 (Figure 1B). The small size confirmed the suitability of the prepared particles for systemic drug delivery.[38] The ζ potential of non-targeted NP/IT was -27.3 mV, while the ζ potential of iNP/IT showed a slight increase of the negative surface charge to -34.1 mV due to the iRGD presence in the particle corona (Table S1). We then confirmed successful co-encapsulation of ICG and TPZ in the nanoparticles. The loading efficiency (LE) of ICG was 12.1% and encapsulation efficiency (EE) of ICG was 80.5%. In contrast, TPZ encapsulation was less efficient with LE of 6.2% and EE of 37%. Absorption spectra of the prepared particles further confirmed co-encapsulation of both drugs as evidenced by the presence of the characteristic peaks at 460 and 779 nm (Figure S1).

Colloidal stability of nanoparticles is a crucial requirement for their systemic intravenous administration.[39] We determined colloidal stability of iNP/IT by incubation with 10% and 50% FBS at 37 °C for 4 h. We have observed no significant size changes during the experiment. The particles retained their original size with no signs of aggregation or precipitation even after storage at 4 °C for 4 weeks (Figure S2). Fluorescence stability of the iNP/IT was also analyzed. Our results showed that even after 7 days, the fluorescence intensity of ICG in iNP/IT remained above 90%, while the fluorescence intensity of free ICG decreased to 38% of the initial value (Figure 1C). These data suggested that iNP/IT possessed suitable stability profile for further investigation.

In vitro drug release from iNP/IT was studied in PBS at 37 °C (Figure 1D). TPZ was released from the nanoparticles with an initial rapid release of ~40% within the first 12 h, which was followed by a continuous slow-release phase. In contrast, ICG showed slow release profile with 70% released after 5 days. These results demonstrated that iNP/IT can achieve sustained release of both ICG and TPZ.

The production of reactive oxygen species (ROS), such as singlet oxygen, plays a major role in PDT by ICG.[40] The ability of the iNP/IT to generate ROS upon NIR laser irradiation was evaluated using DPBF, a probe whose absorption is irreversibly decreased in the presence of singlet oxygen.[41] The absorption of DPBF in iNP/IT solution displayed a continuous decrease to 30% of the initial absorbance upon laser irradiation, indicating singlet oxygen generation (Figure 1E). In contrast, no singlet oxygen was generated in solutions of control empty particles (iNP) or when only laser irradiation in the absence of particles was used (Figure S3).

Enhanced cell uptake of iRGD-conjugated nanoparticles

The effect of iRGD conjugation on the cell uptake of the nanoparticles was evaluated in 4T1 breast cancer cells by flow cytometry (Figure 2A, B). We have used ICG fluorescence to indirectly quantify the uptake of the particles. The results show that after 6 h incubation, the uptake of iNP/IT was significantly higher than uptake of all the control groups. A nearly 2-fold increase in the cell uptake was observed when comparing the iRGD-conjugated

Author Manuscript Author Manuscript Author Manuscript Author Manuscript

particles with the non-targeted NP/IT control (Figure 2A, B). These findings confirm not only successful conjugation of functional iRGD to the particles but also the suitability of this targeting strategy for improved delivery of the ICG/TPZ combination. Confocal microscopy further confirmed the improved uptake of the iRGD-targeted particles (Figure S4). These results demonstrated that iRGD-modified nanoparticles could improve cell uptake ability and enhance cancer cell targeting of cargos, most likely due to the high expression of integrin αvβ3 in 4T1 cells.[11] The enhanced cell uptake of iNP/IT was assumed to improve the eventual performance in antitumor therapy.

Intracellular ROS generation by the nanoparticles

We expected that the conversion of oxygen to ROS by the action of ICG will generate hypoxic conditions in the cells. In such hypoxic microenvironment, TPZ would be activated to induce free radical-mediated oxidative DNA damage and selectively kill hypoxic tumor cells.[42] To verify iNP/IT-mediated ROS generation and the induction of hypoxia in the cancer cells, we treated 4T1 cells with the nanoparticles and analyzed ROS and hypoxia following laser irradiation. As shown in Figure 2C, in comparison with free ICG and NP/IT, the cells treated with iNP/IT exhibited greatly enhanced ROS generation (green) and more pronounced hypoxia (magenta) upon irradiation with the NIR laser. Quantitative analysis using flow cytometry further confirmed this result (Figure S5). Enhanced cell uptake of iNP/IT explains the higher ROS production and subsequent hypoxia generation. These results suggested that treatment with iNP/IT leads to intracellular hypoxia, which is expected to enhance anticancer activity of TPZ.

Anticancer activity of the nanoparticles *in vitro*

To investigate the combined cancer cell killing effect of the codelivered photosensitizer and chemotherapeutic drug, we determined the viability of the 4T1 cells treated with different drug formulations with or without laser irradiation and IC50 values were calculated (Figure 3A, B and C). Considering the oxygen-dependent nature of the two agents and the tumor microenvironment oxygen levels, 20% (normoxia) and 2% (hypoxia) oxygen levels were used in this experiment. As expected, iNP/T exhibited higher cell killing in hypoxia (IC50 10.6 μg/mL) than in normoxia (IC50 23.3 μg/mL) because of the hypoxia-triggered activity of TPZ. In contrast, particles without TPZ (iNP/I) showed decreased cell-killing in hypoxic conditions (hypoxia IC50 17.6 μg/mL, normoxia IC50 14.6 μg/mL). When the two agents were loaded into the same particles (iNP/IT), the cell killing activity was greatly enhanced regardless of the oxygen levels (hypoxia IC50 3.7 μg/mL, normoxia IC50 9.4 μg/mL). Though iNP/I and iNP/IT presented comparable ROS production upon laser irradiation, the combinational cell killing effect of ICG and TPZ effectively improved cytotoxicity of iNP/IT. It is also notable that a mixture of two single-drug-loaded nanoparticles (iNP/T + iNP/I) also showed significant anticancer activity (hypoxia IC50 5.4 μg/mL, normoxia IC50 7.2 μg/mL) when compared with each nanoparticle alone but the activity did not reach the levels of the combination nanoparticles iNP/IT. Thus, iRGD-targeted nanoparticles with co-encapsulated ICG and TPZ show advantage over single drug-loaded nanoparticles, as well as combination of the free drugs and non-targeted nanoparticles. Chou-Talalay isobologram analysis showed that the combination of ICG and TPZ activity in the iNP/IT particles was synergistic. The isobologram method evaluates the interaction at a chosen effect level and is

Author Manuscript Author Manuscript Author Manuscript Author Manuscript

therefore useful to analyze drug combinations. The calculated combination index (CI) offers quantitative descriptor for additive effect (CI = 1), synergism (CI < 1), and antagonism (CI > 1) in drug combinations.[43] The CI values (Figure 3D) showed synergism of the combination under both normoxia and hypoxia as indicated by CI < 1.

The improved anticancer activity of iNP/IT was further corroborated by determining apoptosis in the treated cells using Annexin V analysis (Figure 3E, F). The results showed significant synergistic pro-apoptotic activity of the treatments that combine ICG-mediated PDT and hypoxia-activated TPZ chemotherapeutic effect. All the combination treatments, whether iNP/IT or (iNP/T + iNP/I), showed greatly increased number of apoptotic cells (~90%) and lower proportion of live cells compared with the control groups.

Improved penetration and cell killing activity of iRGD-conjugated nanoparticles in tumor spheroids

The above results confirmed the potential of iNP/IT as efficient formulation with promising anticancer activity in 2D cell culture system. However, evaluation in the 2D cell culture does not allow to predict if the presence of iRGD improves nanoparticle penetration in 3D tumors.[4,44] Considering this, we prepared multicellular tumor spheroids from 4T1 cells and used them as a complementary *in vitro* evaluation system to investigate the penetration of the particles. The penetration was monitored by measuring the fluorescence of the encapsulated ICG using confocal microscopy and the images were converted to surface plots using Image-J (Figure 4A). The highest fluorescence intensity was observed in spheroids treated with iNP/IT. Further analysis confirmed that iNP/IT displayed the deepest penetration in the spheroids with average penetration depth of 89 μm; corresponding to about 12 layers of cells in the spheroids. In contrast, free ICG despite its small size and favorable diffusion properties showed average penetration depth of only 44 μm (~5 cell layers). Surprisingly, non-targeted NP/IT showed depth of ICG penetration of 58 μm, almost 7 layers of cells (Figure 4B). We have used the spheroids as a model of avascular tissue to obtain initial evidence of the nanoparticle tissue-penetrating ability. The achieved penetration depth of 89 μm is highly promising for improved drug delivery in solid tumors after extravasation from the blood vessels. The demonstrated penetration in tumor spheroids of iNP/IT is the direct result of iRGD conjugation and the previously reported three-step targeting and penetrating mechanism of iRGD action, which is associated with αv integrins and neuropilin-1.[10,11]

The cell uptake of nanoparticles in the spheroids was measured next by analyzing the ICG fluorescence in single cell suspension prepared from the spheroids using flow cytometry (Figure 4C, D). Consistent with the above results, the cells in the iNP/IT-treated group possessed the highest uptake as indicated by almost 4-fold higher ICG fluorescence per cell when compared with the control mixture of free iRGD and NP/IT. The fraction of cells that have taken up the particles was also significantly higher in the iNP/IT group than all the other groups (>7-fold). These results indicated that iRGD conjugation could increase uptake of the nanoparticles in the tumor spheroids and result in improved drug delivery efficiency. Based on the confocal microscopy observations and flow cytometry analysis, we found that

Author Manuscript Author Manuscript Author Manuscript Author Manuscript

iRGD-conjugated nanoparticles promoted inward distribution and accumulation of the encapsulated drugs in the tumor spheroids.

The robust spheroid penetration of iNP/IT endowed them with a higher likelihood to gain access to increased number of cancer cells and to boost cell internalization and cell killing efficacy. The partial hypoxic environment in tumor spheroids was also advantageous for TPZ to exhibit specific toxicity (Figure S6). This hypothesis was tested in the subsequent live/dead assay in the spheroids treated with the nanoparticles with or without laser irradiation (Figure 4E, S7). In this assay, live cells were indicated by green fluorescence and dead cells by red fluorescence. The control untreated spheroids showed only a limited number of dead cells mostly due to necrosis in the core of the spheroids. In contrast, treatment with iNP/IT combined with laser irradiation resulted in a large number of dead cells throughout the spheroids and only a limited number of live cells remaining. Similar results were also observed in spheroids treated with a combination of single-agent particles (iNP/T + iNP/I). To study the induction of apoptosis in individual cells, we have digested the spheroids to single-cell suspension, which was then analyzed by flow cytometry (Figure S8). Both iNP/IT and (iNP/T + iNP/I) treatments significantly increased the fraction of apoptotic and necrotic cells (~85%) compared with the other tested treatments. These *in vitro* results suggested that iRGD-modified nanoparticles could not only enhance tumor penetration, but could also facilitate cell internalization and promote cell death within the 3D environment of the spheroids. Additionally, these results provided initial evidence that the nanoparticle could be used to achieve combined PDT and hypoxia-activated therapy, a prerequisite for the success of the *in vivo* tumor treatment studies.

In vivo tumor accumulation and penetration

Following the promising *in vitro* findings, we set to explore whether the iRGD-containing nanoparticles also improved delivery and penetration in solid tumors *in vivo*. The nanoparticles were administered intravenously into mice bearing orthotopic 4T1 tumors and whole-body fluorescence imaging was performed at different time points to capture the distribution of the ICG-containing particles. As expected, free ICG distributed mainly to the liver and its fluorescence signal decayed rapidly as a result of aggregation and clearance from the body (Figure 5A).[45] In contrast, strong fluorescence signal was detected in the tumors of mice treated with iNP/IT as early as 4 h after injection. The tumor accumulation increased with increasing time, suggesting that the iNP/IT remained in circulation and could accumulate into the tumor effectively. After 48 h, iNP/IT were still retained in the tumor tissue. In mice treated with the non-targeted NP/IT and with a mixture of NP/IT and free iRGD peptide, strong fluorescence was observed in the liver. Comparatively less fluorescence was found in the tumor at 4 h and most body fluorescence disappeared within 48 h. Following animal sacrifice, we measured *ex vivo* fluorescence of the excised tissues to validate the whole-body imaging data. We indeed found significantly higher fluorescence in the tumors of mice treated with iNP/IT and comparatively less accumulation in the liver when compared to other treatments (Figure 5B, C). To evaluate the ability of the iRGD-containing nanoparticles to penetrate deep into the tumors, we stained tumor blood vessels with anti-CD31 antibody (Figure 5D, green). Consistent with the spheroid findings and with the *in vivo* imaging data, iNP/IT spread more widely from the blood vessels than the other

Author Manuscript Author Manuscript Author Manuscript Author Manuscript

treatments. We estimated that the distance between blood vessels in the 4T1 tumors ranged from about fifty to several hundred μm. This was consistent with previous reports showing similar range of intercapillary distance in various solid tumor models.[46-48] Thus, the penetration ability of the iNP/IT nanoparticles appears sufficient to greatly enhance distribution in the tumors following extravasation from the blood vessels.

As shown in Figure 3, TPZ requires hypoxia for its full activation and chemotherapeutic activity. To confirm that the 4T1 tumor model was suitable for testing the hypoxia-activated TPZ mechanism of action, we measured the extent of hypoxia in the 4T1 tumor microenvironment by pimonidazole staining in frozen tumor tissue sections. Pimonidazole is a well-characterized exogenous hypoxia marker, which forms protein adducts under hypoxic conditions that can be visualized by immunohistochemical staining following animal sacrifice.[49] As shown in Figure 5E, hypoxic areas were heterogeneously distributed throughout the 4T1 tumor. The fluorescence signal of iNP/IT was widely distributed and to a significant extent co-localized with the hypoxic areas. These results confirmed the existence of hypoxia in the 4T1 tumors and showed the ability of iNP/IT to reach the hypoxic regions.

In vivo antitumor efficacy

The greatly enhanced tumor accumulation and intratumoral penetration provided us with strong rationale to evaluate antitumor activity of the iRGD-targeted nanoparticles *in vivo*. To validate the merits of the combination therapy using our tumor-penetrating nanoparticles, the evaluation was performed in metastatic orthotopic 4T1 mammary adenocarcinoma model. As shown in Figure 6A, fast tumor growth was observed in the control untreated group, while moderately restricted tumor growth was achieved using iRGD-targeted nanoparticles loaded with a single drug (iNP/I and iNP/T), combination of free drugs (ICG+TPZ), as well as in mice treated with the non-penetrating nanoparticles (NP/IT). We observed the strongest antitumor effect with iNP/IT as evidenced by the nearly complete elimination of the primary orthotopic tumors due to the synergistic effect of the ICG-mediated PDT and the hypoxia-activated TPZ chemotherapy. Combination treatment with the single-drug loaded nanoparticles (iNP/I + iNP/T) showed the second best antitumor effect. The superiority of the iNP/IT treatment, further confirmed the benefits of co-delivering drug combinations in a single nanoparticle formulation as opposed to using individual single-drug nanoparticles. Mice were sacrificed on day 13 and excised tumors weighted and photographed. The analysis confirmed that iNP/IT was the most effective in suppressing tumor growth (Figure 6B). The body weight of mice from each group was not significantly affected by any of the treatments, suggesting no major toxicity (Figure S9). Moreover, the H&E staining of tissue sections of major organs showed no obvious tissue damage when compared to the untreated group (Figure S10).

Analysis of the H&E tumor sections suggested considerably enhanced necrosis in the iNP/IT group (~95% necrotic area) when compared with the control groups (~30% necrotic area). Immunohistochemical staining of the tumor sections for Ki-67 antigen was used to evaluate the extent of tumor cell proliferation (Figure 6C). Visually, tumor cells in the iNP/IT treated group exhibited decreased Ki-67 expression, indicating markedly reduced tumor cell

Author Manuscript Author Manuscript Author Manuscript Author Manuscript

proliferation after treatment.[50,51] Hot-spot analysis confirmed the significance of the results (Figure 6D).

The orthotopic 4T1 model used in the therapeutic study spontaneously forms lung metastases. Thus, we also evaluated if the iNP/IT treatment showed antimetastatic effect. The antimetastatic activity was assessed by analyzing the number of surface lung metastases and subsequent analysis of lung H&E tissue sections. As shown in Figure 6E and F, iNP/IT treatment resulted in a significantly decreased number of surface lung metastatic lesions compared with the control groups. This finding was further corroborated by the analysis of the lung tissue sections which also showed markedly decreased metastasis in the lungs of animals treated with iNP/IT. Thus, iNP/IT treatment not only effectively suppressed primary tumor growth but also successfully inhibited tumor metastasis.

Conclusion

In this study, we have reported successful development of iRGD-modified nanoparticles, which could simultaneously deliver ICG and TPZ to solid tumors for combined PDT and hypoxia-activated chemotherapy against metastatic breast cancer. Conjugation of iRGD peptide to the nanoparticles significantly enhanced the accumulation and penetration of the loaded drugs in both cell monolayer and multicellular spheroids. iNP/IT demonstrated remarkable antitumor efficacy in metastatic 4T1 tumor model, owing to the synergistic effect of ICG-mediated PDT and hypoxia-triggered TPZ treatment. Antimetastatic activity was also achieved during the treatment. The nanoparticles presented here provide an effective strategy for enhanced anticancer therapy.

Materials and Methods

Materials

Poly (D, L-lactide-co-glycolide) (PLGA, MW 7-17K), tirapazamine (TPZ) and 1,3-diphenylisobenzofuran (DPBF) were obtained from Sigma Aldrich (St. Louis, MO). Indocyanine green (ICG) was purchased from Polysciences (Warrington, PA). 1,2-distearoyl-sn-glycero-3-phosphoethanol-amine-*N*-[methyl ether (polyethylene glycol)-2000] (DSPE-mPEG) was obtained from Laysan Bio (Arab, AL). 1,2-dipalmitoyl-sn-glycero-3-phosphocholine(DPPC) and 1,2-distearoyl-*sn*-glycero-3-phospho-ethanolamine-*N*-[dibenzocyclooctyl (polyethylene glycol)-2000] (DSPE-PEG-DBCO) was purchased from Avanti (Alabaster, AL). N-terminal azido-functionalized iRGD peptide (N3-Ac (CRGDKGPDC)) was custom-synthesized by GL Biochem (Shanghai, China). Phosphate-buffered saline (PBS), Dulbecco's Modified Eagle Medium (DMEM), sodium pyruvate, essential amino acids and non-essential amino acids were from Hyclone (Logan, UT). Fetal bovine serum (FBS) was from Atlanta Biologicals (Flowery Branch, GA). Gentamicin was purchased from Gibco (Life Technologies, Grand Island, NY). Centrifugal filter Vivaspin20 (MWCO 10 kDa) was purchased from GE healthcare (Buckinghamshire, UK). All other reagents were from Fisher Scientific and used as received unless otherwise noted.

Author Manuscript Author Manuscript Author Manuscript Author Manuscript

Cell Culture

Mouse breast carcinoma 4T1 was a kind gift from Dr. Fred Miller (Wayne State University) and cultured in DMEM supplemented with 2 mM L-glutamine, 1 mM sodium pyruvate, essential amino acids, non-essential amino acids, gentamycin (0.2 mg/mL) and 10% FBS. The cells were grown at 37°C with 5% CO_2 in a humidified chamber.

Preparation of nanoparticles

Nanoparticles containing ICG and TPZ (NP/IT) were prepared by a modified single-step nanoprecipitation method.[52] PLGA (5 mg/mL) was dissolved in acetone, ICG (2 mg/mL) was dissolved in water, and TPZ (1 mg/mL) was dissolved in methanol. Stock solutions of DPPC, DSPE-PEG, and DSPE-PEG-DBCO were prepared separately at 1 mg/mL in 4% ethanol aqueous solution. The mixed lipid solution was heated to 65 °C under gentle stirring to ensure that all lipids were in liquid phase. ICG and TPZ (1:1, w/w) were added to the PLGA solution and mixed thoroughly. Then, the PLGA solution and DPPC/DSPE-PEG/DSPE-PEG-DBCO (4:3:3, w/w) with a total mass ratio of 15% to PLGA polymer, were added dropwise to deionized water under sonication for 20 min. The formed particles were washed three times using a Vivaspin 20 centrifugal filter. The same procedure was used to prepare control nanoparticles containing only ICG (NP/ICG) and TPZ (NP/TPZ). To prepare iRGD-modified nanoparticles, azido-functionalized iRGD (equal molar ratio to DSPE-PEG-DBCO) was added to nanoparticle aqueous solution. After reaction at 37°C for 30 min, the iRGD-nanoparticle (iNP) were collected by centrifugation and washing with water.

Nanoparticle characterization

Hydrodynamic diameter, polydispersity, and zeta potential of the nanoparticles were determined by dynamic light scattering (DLS) using a ZEN3600 Zetasizer Nano-ZS (Malvern Instruments Ltd., Massachusetts, USA). Morphological observation was performed under transmission electron microscopy (TEM, Tecnai G2 Spirit, FEI Company, USA) using negative staining (Nanoprobes, USA).

The LE and EE of ICG and TPZ in the nanoparticles were measured as follows. Following preparation, the nanoparticles were centrifuged at 25,000 rpm for 30 min and free ICG and TPZ in the supernatant were measured by a microplate reader at 776 nm and 460 nm, respectively. The LE and EE were calculated as: LE (%) = ((weight of loaded drug)/(total weight of nanoparticles)) ×100; EE (%) = ((weight of loaded drug)/(weight of initially added drug))×100. The absorption spectra of ICG, TPZ and NP/IT and fluorescence intensity of ICG were also measured by the microplate reader.

In vitro drug release was determined as follows. The nanoparticles were suspended in PBS (pH 7.4) in microcentrifuge tubes and kept in a shaking incubator at 37°C. At predetermined time points, aliquots were taken out and centrifuged at 14,000 rpm for 5 min. The supernatant was collected and the ICG concentration in the supernatant was measured by fluorescence intensity (FL) with the microplate reader (exc/em 740/815 nm). The TPZ concentration was measured by UV absorbance in the microplate reader as described above.

Author Manuscript Author Manuscript Author Manuscript Author Manuscript

DPBF, as an indicator to investigate the generation of $^1O_2$, could react irreversibly with $^1O_2$ to cause a reduction in its absorbance. Briefly, DPBF in ethanol (20 μL, 5 mM) was added to a solution of iNP/IT (ICG, 30 μg/mL) in 1 mL aqueous solution. The solution was then irradiated with 808 nm laser (2 W/cm^2, Meig Waei, China). After the designated time intervals of near-infrared (NIR)-laser irradiation, the absorption spectra of the mixture were measured by the microplate reader.

Cell uptake and ROS analysis

Flow cytometry was used to study the cellular uptake of nanoparticles *in vitro*. 4T1 cells were seeded in 12-well plates at the density of 1×10^5 cells/well and incubated with either free ICG or the nanoparticles (ICG, 30 μg/mL) for 6 h. The cells were harvested and cell uptake determined from ICG fluorescence per cell using a BD FACSCalibur flow cytometer (Bedford, MA) and FlowJo software for analysis.

Intracellular ROS and hypoxia were measured using the ROS-ID® Hypoxia/Oxidative stress detection kit (Enzo Life Sciences). 4T1 cells were cultured in a 20-mm glass-bottom dish (Nest) (3×10^4 cells/dish) and grown in complete medium for 24 h before treatment. Cells were treated with free ICG, NP/IT and iNP/IT (ICG, 30 μg/mL) for 6 h and treated with the kit reagent mix according to the manufacturer's instructions. After 30 min, the cells were washed twice and exposed to 808 nm laser irradiation for 3 min. Laser was placed on the top of dishes or plates during irradiation in all the cell experiment. After irradiation, cells were washed, stained by Hoechst 33258, and observed by LSM 710 laser scanning confocal microscope (Zeiss, Jena, Germany).

Cytotoxicity and apoptosis assay

4T1 cells (3×10^3 cells/well) were cultured in normal oxygen levels (20%) for 12 h and then transferred to an incubator with either 2% or 20% oxygen atmosphere for an additional 24 h. The cells were treated with increasing concentrations of the nanoparticles (total drug dose 1.50 - 18.75 μg/mL, ICG:TPZ=2:1) and exposed to a 3-min laser irradiation, followed by incubation for an additional 24 h. Cell viability was evaluated by Cell Titer Blue assay. The relative cell viability was normalized to the viability of untreated cells and expressed as the means ± SD of triplicate samples.

Apoptosis was examined using the Annexin V-FITC/PI Apoptosis Detection Kit (BioLegend, USA). Briefly, the cells were seeded in 12-well plates at the density of 1×10^5 cells per well and cultured at different oxygen levels (2, 20%) as described above. At the 80% confluency, the cells were treated with the nanoparticles followed by a 3-min laser irradiation and incubation for an additional 24 h. The Annexin V-FITC apoptosis detection was performed using flow cytometry in accordance with the manufacturer's protocol and the data were processed using FlowJo.

Nanoparticle activity in multicellular tumor spheroids

The 4T1 cells (5×10^6 in 15 mL of complete media) were added to a 2% agarose-coated Petri dish and grown at 37 °C. The growth of spheroids was monitored with an EVOS fluorescence microscope (AMG). When the spheroid size reached 400 μm, free ICG or the

Author Manuscript Author Manuscript Author Manuscript Author Manuscript

nanoparticles (ICG, 30 μg/mL) was added and the spheroids were cultured for another 12 h. After washing and fixing in 4% paraformaldehyde, the ICG fluorescence in spheroids was measured with the confocal microscope using XY-stack with 10 μm intervals. The images were also analyzed using ImageJ software. The spheroids were then treated trypsin, the obtained single-cell suspension washed with PBS and subjected to flow cytometry analysis.

The cytotoxicity of the nanoparticles in the spheroids was determined using a Live/Dead Viability/Cytotoxicity Kit (Biotium, USA). The 4T1 spheroids with 400 μm diameter were incubated with the nanoparticles (total drug dose, 7.5 μg/mL, ICG: TPZ=2:1) with or without laser irradiation for 3 min. After 12 h incubation, spheroids were rinsed with PBS and treated per manufacturer's protocol. Images were obtained with the confocal microscope. Apoptosis was also examined using the Annexin V-FITC/PI Apoptosis Detection Kit by flow cytometry. Hypoxia in the spheroids was evaluated using the ROS-ID® Hypoxia/Oxidative stress detection kit (Enzo Life Sciences).

In vivo biodistribution of nanoparticles

All animal experiments followed a protocol approved by the Institutional Animal Care and Use Committee. Biodistribution of the nanoparticles in tumor-bearing mice was analyzed by whole-body fluorescence imaging. 4T1 cells (5×10^5) were injected into the mammary fat pad of female Balb/c mice. When the tumor reached 150–200 mm^3, free ICG or nanoparticles were administered *via* tail injection (100 μL, ICG concentration 100 μg/mL). At 4, 24 and 48 h after administration, mice were anesthetized and imaged using Xenogen IVIS 200. The mice were sacrificed 48 h post-administration and the tumors and major organs were harvested and subjected to *ex vivo* fluorescence imaging. The fluorescence from each organ was analyzed by the instrument software. Then, the isolated tumors were embedded in OCT compound, cut into 10 μm sections, and stained with DAPI. Blood vessels in the tumor frozen sections were visualized by confocal microscopy using CD31 antibody staining (Abcam, ab28364). Tumor hypoxia was analyzed 48 h post-injection using pimonidazole hydrochloride (60 mg/kg) given by intraperitoneal injection. The mice were sacrificed 30 min after pimonidazole injection and the tumors were excised and frozen tumor sections were stained with FITC-Mab1 antibody using the Hypoxyprobe-1 Plus Kit (Hypoxyprobe Inc., Burlington) and imaged with the confocal microscope.

In vivo therapeutic efficacy

Orthotopic 4T1 tumors were established as above and treatment commenced when the average tumor volume reached about 100 mm^3. A total of 35 female Balb/c mice (8 weeks old) were randomly assigned into seven groups (n=5) and injected with 5% glucose, free ICG controls, or various nanoparticle formulations *via* tail vein (2.5 mg/kg ICG, 1.2 mg/kg TPZ) at day 2 and 5. All the ICG-treated groups received 5-min laser irradiation at day 3 and 6 (laser was placed ~1 cm above the tumor). Tumor growth was monitored by digital calipers and the volumes calculated as: tumor volume (mm^3) = 0.5 × length × $width^2$. Body weight of the mice was recorded daily. All the mice were sacrificed on day 14 and the tumors were collected, weighed, and used for H&E and Ki-67 staining. For Ki-67 immunostaining, antigen retrieval was performed using discovery CC1 solution (Ventana) at 95°C (pH 8.5). Primary antibody (Abcam, ab16667) was incubated for 32 min at 37°C with

Author Manuscript Author Manuscript Author Manuscript Author Manuscript

dilution of 1:200. Following staining, sections were observed using a microscope to obtain the proliferation index (percentage of Ki67-positive cells from the total cells). Three fields with the highest density of immunolabelled tumor cell nuclei ('hot-spot') were assessed per tumor at 40× magnification. The lungs were inflated with 30% sucrose, fixed in Bouin's solution for 18 h, and stored in 70% ethanol. Each of the five pulmonary lobes was separated and surface tumors were counted under dissecting microscope. After counting, the lungs were sectioned and stained with H&E. Other major organs, including heart, liver, spleen and kidneys were also harvested, fixed in 4% paraformaldehyde, sectioned and stained with H&E. Blinded histological analysis of the tissues was conducted by a trained pathologist at the UNMC core facility.

Statistical Analysis

Data are presented as the means ± SD. The statistical significance was determined using ANOVA followed by Bonferroni *post hoc* correction with $p < 0.05$ as the minimal level of significance.

Supplementary Material

Refer to Web version on PubMed Central for supplementary material.

Acknowledgments

Financial support from the University of Nebraska Medical Center, National Institutes of Health (EB015216, EB020308, EB019175), China Scholarship Council (YW, YX), and Changjiang Scholar Program (DO) is gratefully acknowledged.

References

1. Yu H, Cui Z, Yu P, Guo C, Feng B, Jiang T, Wang S, Yin Q, Zhong D, Yang X. pH-and NIR Light-Responsive Micelles with Hyperthermia-Triggered Tumor Penetration and Cytoplasm Drug Release to Reverse Doxorubicin Resistance in Breast Cancer. Adv Funct Mater. 2015; 25:2489–2500.
2. Liu Y, Zhang D, Qiao ZY, Qi GB, Liang XJ, Chen XG, Wang H. A Peptide - Network Weaved Nanoplatform with Tumor Microenvironment Responsiveness and Deep Tissue Penetration Capability for Cancer Therapy. Adv Mater. 2015; 27:5034–5042. [PubMed: 26198072]
3. Zhu L, Kate P, Torchilin VP. Matrix Metalloprotease 2-Responsive Multifunctional Liposomal Nanocarrier for Enhanced Tumor Targeting. ACS Nano. 2012; 6:3491–3498. [PubMed: 22409425]
4. Ni D, Ding H, Liu S, Yue H, Bao Y, Wang Z, Su Z, Wei W, Ma G. Superior Intratumoral Penetration of Paclitaxel Nanodots Strengthens Tumor Restriction and Metastasis Prevention. Small. 2015; 11:2518–2526. [PubMed: 25678130]
5. Wilhelm S, Tavares AJ, Dai Q, Ohta S, Audet J, Dvorak HF, Chan WCW. Analysis of Nanoparticle Delivery to Tumours. Nat Rev Mater. 2016; 1:16014.
6. Prabhakar U, Maeda H, Jain RK, Sevick-Muraca EM, Zamboni W, Farokhzad OC, Barry ST, Gabizon A, Grodzinski P, Blakey DC. Challenges and Key Considerations of the Enhanced Permeability and Retention Effect for Nanomedicine Drug Delivery in Oncology. Cancer Res. 2013; 73:2412–2417. [PubMed: 23423979]
7. Feig C, Gopinathan A, Neesse A, Chan DS, Cook N, Tuveson DA. The Pancreas Cancer Microenvironment. Clin Cancer Res. 2012; 18:4266–4276. [PubMed: 22896693]
8. Wong C, Stylianopoulos T, Cui J, Martin J, Chauhan VP, Jiang W, Popović Z, Jain RK, Bawendi MG, Fukumura D. Multistage Nanoparticle Delivery System for Deep Penetration into Tumor Tissue. Proc Natl Acad Sci U S A. 2011; 108:2426–2431. [PubMed: 21245339]

Author Manuscript Author Manuscript Author Manuscript Author Manuscript

9. Brown JM, Wilson WR. Exploiting Tumour Hypoxia in Cancer Treatment. Nat Rev Cancer. 2004; 4:437–447. [PubMed: 15170446]
10. Sugahara KN, Teesalu T, Karmali PP, Kotamraju VR, Agemy L, Greenwald DR, Ruoslahti E. Coadministration of a Tumor-Penetrating Peptide Enhances the Efficacy of Cancer Drugs. Science. 2010; 328:1031–1035. [PubMed: 20378772]
11. Sugahara KN, Teesalu T, Karmali PP, Kotamraju VR, Agemy L, Girard OM, Hanahan D, Mattrey RF, Ruoslahti E. Tissue-Penetrating Delivery of Compounds and Nanoparticles into Tumors. Cancer Cell. 2009; 16:510–520. [PubMed: 19962669]
12. Ruoslahti E. Tumor Penetrating Peptides for Improved Drug Delivery. Adv Drug Delivery Rev. 2016; doi: 10.1016/j.addr.2016.03.008
13. Akashi Y, Oda T, Ohara Y, Miyamoto R, Kurokawa T, Hashimoto S, Enomoto T, Yamada K, Satake M, Ohkohchi N. Anticancer Effects of Gemcitabine Are Enhanced by Co-Administered iRGD Peptide in Murine Pancreatic Cancer Models That Overexpressed Neuropilin-1. Br J Cancer. 2014; 110:1481–1487. [PubMed: 24556620]
14. Khawar IA, Kim JH, Kuh HJ. Improving Drug Delivery to Solid Tumors: Priming the Tumor Microenvironment. J Controlled Release. 2015; 201:78–89.
15. Dolmans DE, Fukumura D, Jain RK. Photodynamic Therapy for Cancer. Nat Rev Cancer. 2003; 3:380–387. [PubMed: 12724736]
16. Idris NM, Gnanasammandhan MK, Zhang J. *In Vivo* Photodynamic Therapy Using Upconversion Nanoparticles as Remote-Controlled Nanotransducers. Nat Med. 2012; 18:1580–1585. [PubMed: 22983397]
17. Samia AC, Chen X, Burda C. Semiconductor Quantum Dots for Photodynamic Therapy. J Am Chem Soc. 2003; 125:15736–15737. [PubMed: 14677951]
18. Barth BM, I Altinoğlu E, Shanmugavelandy SS, Kaiser JM, Crespo-Gonzalez D, DiVittore NA, McGovern C, Goff TM, Keasey NR, Adair JH. Targeted Indocyanine-Green-Loaded Calcium Phosphosilicate Nanoparticles for *In Vivo* Photodynamic Therapy of Leukemia. ACS Nano. 2011; 5:5325–5337. [PubMed: 21675727]
19. Fingar VH, Wieman TJ, Wiehle SA, Cerrito PB. The Role of Microvascular Damage in Photodynamic Therapy: The Effect of Treatment on Vessel Constriction, Permeability, and Leukocyte Adhesion. Cancer Res. 1992; 52:4914–4921. [PubMed: 1387584]
20. Gallagher W, Allen L, O'Shea C, Kenna T, Hall M, Gorman A, Killoran J, O'Shea D. A Potent Nonporphyrin Class of Photodynamic Therapeutic Agent: Cellular Localisation, Cytotoxic Potential and Influence of Hypoxia. Br J Cancer. 2005; 92:1702–1710. [PubMed: 15841085]
21. Busch TM, Hahn SM, Evans SM, Koch CJ. Depletion of Tumor Oxygenation During Photodynamic Therapy: Detection by the Hypoxia Marker EF3 [2-(2-Nitroimidazol-1 [H]-YL)-N-(3, 3, 3-Trifluoropropyl) Acetamide]. Cancer Res. 2000; 60:2636–2642. [PubMed: 10825135]
22. Cheng Y, Cheng H, Jiang C, Qiu X, Wang K, Huan A, Yuan A, Wu J, Hu Y. Perfluorocarbon Nanoparticles Enhance Reactive Oxygen Levels and Tumour Growth Inhibition in Photodynamic Therapy. Nat Commun. 2015; 6:8785–8785. [PubMed: 26525216]
23. Kumar R, Kim EJ, Han J, Lee H, Shin WS, Kim HM, Bhuniya S, Kim JS, Hong KS. Hypoxia-Directed and Activated Theranostic Agent: Imaging and Treatment of Solid Tumor. Biomaterials. 2016; 104:119–128. [PubMed: 27449948]
24. Tian J, Cheng N, Liu Q, Xing X, Sun X. Cobalt Phosphide Nanowires: Efficient Nanostructures for Fluorescence Sensing of Biomolecules and Photocatalytic Evolution of Dihydrogen from Water Under Visible Light. Int Ed Engl. 2015; 54:5493–5497.
25. Chen H, Tian J, He W, Guo Z. H_2O_2-Activatable and O_2-Evolving Nanoparticles for Highly Efficient and Selective Photodynamic Therapy Against Hypoxic Tumor Cells. J Am Chem Soc. 2015; 137:1539–1547. [PubMed: 25574812]
26. Zhang C, Zhao K, Bu W, Ni D, Liu Y, Feng J, Shi J. Marriage of Scintillator and Semiconductor for Synchronous Radiotherapy and Deep Photodynamic Therapy with Diminished Oxygen Dependence. Angew Chem Int Ed Engl. 2015; 127:1790–1794.
27. Gupta MK, Martin JR, Werfel TA, Shen T, Page JM, Duvall CL. Cell Protective, ABC Triblock Polymer-Based Thermoresponsive Hydrogels with ROS-Triggered Degradation and Drug Release. J Am Chem Soc. 2014; 136:14896–14902. [PubMed: 25254509]

Author Manuscript Author Manuscript Author Manuscript Author Manuscript

28. Chen Q, Feng L, Liu J, Zhu W, Dong Z, Wu Y, Liu Z. Intelligent Albumin – MnO_2 Nanoparticles as pH - /H_2O_2 - Responsive Dissociable Nanocarriers to Modulate Tumor Hypoxia for Effective Combination Therapy. Adv Mater. 2016; 28:7129–7136. [PubMed: 27283434]
29. Bremner J, Adams G, Pearson J, Sansom J, Stratford I, Bedwell J, Bown S, MacRobert A, Phillips D. Increasing the Effect of Photodynamic Therapy on the RIF-1 Murine Sarcoma, Using the Bioreductive Drugs RSU1069 and RB6145. Br J Cancer. 1992; 66:1070. [PubMed: 1457346]
30. Feng L, Cheng L, Dong Z, Tao D, Barnhart TE, Cai W, Chen M, Liu Z. Theranostic Liposomes with Hypoxia-Activated Prodrug to Effectively Destruct Hypoxic Tumors Post Photodynamic Therapy. ACS Nano. 2016; doi: 10.1021/acsnano.6b07525
31. Brown JM. Exploiting the Hypoxic Cancer Cell: Mechanisms and Therapeutic Strategies. Mol Med Today. 2000; 6:157–162. [PubMed: 10740254]
32. Peters KB, Brown JM. Tirapazamine: A Hypoxia-Activated Topoisomerase II Poison. Cancer Res. 2002; 62:5248–5253. [PubMed: 12234992]
33. Reddy SB, Williamson SK. Tirapazamine: A Novel Agent Targeting Hypoxic Tumor Cells. Expert Opin Invest Drugs. 2009; 18:77–87.
34. Su S, Tian Y, Li Y, Ding Y, Ji T, Wu M, Wu Y, Nie G. "Triple-Punch" Strategy for Triple Negative Breast Cancer Therapy with Minimized Drug Dosage and Improved Antitumor Efficacy. ACS Nano. 2015; 9:1367–1378. [PubMed: 25611071]
35. Li Y, Wen T, Zhao R, Liu X, Ji T, Wang H, Shi X, Shi J, Wei J, Zhao Y. Localized Electric Field of Plasmonic Nanoplatform Enhanced Photodynamic Tumor Therapy. ACS Nano. 2014; 8:11529–11542. [PubMed: 25375193]
36. Ogawa M, Kosaka N, Choyke PL, Kobayashi H. *In Vivo* Molecular Imaging of Cancer with a Quenching Near-Infrared Fluorescent Probe Using Conjugates of Monoclonal Antibodies and Indocyanine Green. Cancer Res. 2009; 69:1268–1272. [PubMed: 19176373]
37. Zhang L, Chan JM, Gu FX, Rhee JW, Wang AZ, Radovic-Moreno AF, Alexis F, Langer R, Farokhzad OC. Self-Assembled Lipid– Polymer Hybrid Nanoparticles: A Robust Drug Delivery Platform. ACS Nano. 2008; 2:1696–1702. [PubMed: 19206374]
38. Torchilin V. Tumor Delivery of Macromolecular Drugs Based on the EPR Effect. Adv Drug Delivery Rev. 2011; 63:131–135.
39. Ding Y, Wang Y, Opoku-Damoah Y, Wang C, Shen L, Yin L, Zhou J. Dual-Functional Bio-Derived Nanoparticulates for Apoptotic Antitumor Therapy. Biomaterials. 2015; 72:90–103. [PubMed: 26344366]
40. Liu Y, Liu Y, Bu W, Cheng C, Zuo C, Xiao Q, Sun Y, Ni D, Zhang C, Liu J. Hypoxia Induced by Upconversion-Based Photodynamic Therapy: Towards Highly Effective Synergistic Bioreductive Therapy in Tumors. Angew Chem Int Ed Engl. 2015; 127:8223–8227.
41. Wang T, Zhang L, Su Z, Wang C, Liao Y, Fu Q. Multifunctional Hollow Mesoporous Silica Nanocages for Cancer Cell Detection and the Combined Chemotherapy and Photodynamic Therapy. ACS Appl Mater Interfaces. 2011; 3:2479–2486. [PubMed: 21604817]
42. Denny WA, Wilson WR. Tirapazamine: A Bioreductive Anticancer Drug That Exploits Tumour Hypoxia. Expert Opin Invest Drugs. 2000; 9:2889–2901.
43. Chou TC. Drug Combination Studies and Their Synergy Quantification Using the Chou-Talalay Method. Cancer Res. 2010; 70:440–446. [PubMed: 20068163]
44. Peng ZH, Kopecek J. Enhancing Accumulation and Penetration of HPMA Copolymer–Doxorubicin Conjugates in 2D and 3D Prostate Cancer Cells *via* iRGD Conjugation with an MMP-2 Cleavable Spacer. J Am Chem Soc. 2015; 137:6726–6729. [PubMed: 25963409]
45. Zheng M, Yue C, Ma Y, Gong P, Zhao P, Zheng C, Sheng Z, Zhang P, Wang Z, Cai L. Single-Step Assembly of DOX/ICG Loaded Lipid–Polymer Nanoparticles for Highly Effective Chemo-Photothermal Combination Therapy. ACS Nano. 2013; 7:2056–2067. [PubMed: 23413798]
46. Robinson SP, Rijken PF, Howe FA, McSheehy PM, van der Sanden BP, Heerschap A, Stubbs M, van der Kogel AJ, Griffiths JR. Tumor Vascular Architecture and Function Evaluated by Non-Invasive Susceptibility MRI Methods and Immunohistochemistry. J Magn Reson Imaging. 2003; 17:445–454. [PubMed: 12655584]
47. Yoshii Y, Sugiyama K. Intercapillary Distance in the Proliferating Area of Human Glioma. Cancer Res. 1988; 48:2938–2941. [PubMed: 3359450]

Author Manuscript Author Manuscript Author Manuscript Author Manuscript

48. Manzoor AA, Lindner LH, Landon CD, Park JY, Simnick AJ, Dreher MR, Das S, Hanna G, Park W, Chilkoti A. Overcoming Limitations in Nanoparticle Drug Delivery: Triggered, Intravascular Release to Improve Drug Penetration into Tumors. Cancer Res. 2012; 72:5566–5575. [PubMed: 22952218]

49. Cao Y, Li CY, Moeller BJ, Yu D, Zhao Y, Dreher MR, Shan S, Dewhirst MW. Observation of Incipient Tumor Angiogenesis That Is Independent of Hypoxia and Hypoxia Inducible Factor-1 Activation. Cancer Res. 2005; 65:5498–5505. [PubMed: 15994919]

50. Lopez XM, Debeir O, Maris C, Rorive S, Roland I, Saerens M, Salmon I, Decaestecker C. Clustering Methods Applied in the Detection of Ki67 Hot-Spots in Whole Tumor Slide Images: An Efficient Way to Characterize Heterogeneous Tissue-Based Biomarkers. Cytometry, Part A. 2012; 81:765–775.

51. Ma M, Huang Y, Chen H, Jia X, Wang S, Wang Z, Shi J. Bi_2S_3-Embedded Mesoporous Silica Nanoparticles for Efficient Drug Delivery and Interstitial Radiotherapy Sensitization. Biomaterials. 2015; 37:447–455. [PubMed: 25453972]

52. Fang RH, Aryal S, Hu CMJ, Zhang L. Quick Synthesis of Lipid-Polymer Hybrid Nanoparticles with Low Polydispersity Using a Single-Step Sonication Method. Langmuir. 2010; 26:16958–16962. [PubMed: 20961057]

Author Manuscript Author Manuscript Author Manuscript Author Manuscript

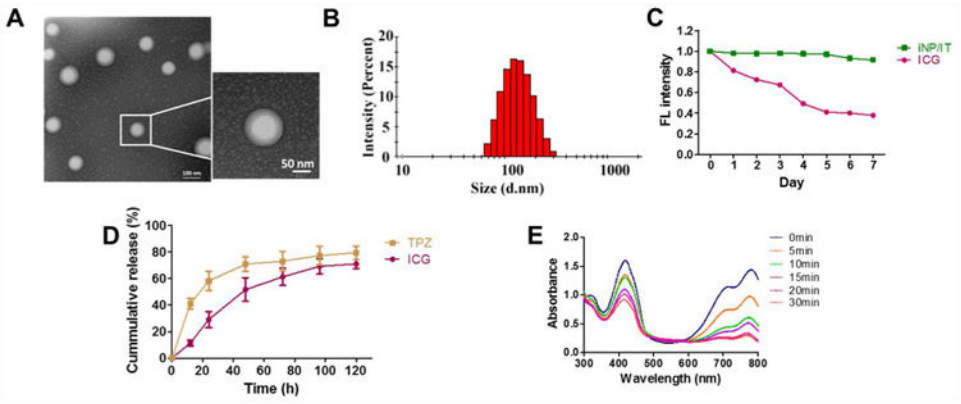

Figure 1.

Nanoparticle characterization. (A) TEM images of iNP/IT. (B) DLS size distribution of iNP/IT. (C) Fluorescence stability of iNP/IT and free ICG in water. (D) Release profiles of ICG and TPZ from iNP/IT in PBS at 37 °C. The data are shown as mean ± SD (n = 3) (E) ROS generation by iNP/IT. Normalized UV/vis absorption spectra iNP/IT with DPBF single oxygen probe after irradiation with 808 nm laser (2 W/cm^2).

Author Manuscript Author Manuscript Author Manuscript Author Manuscript

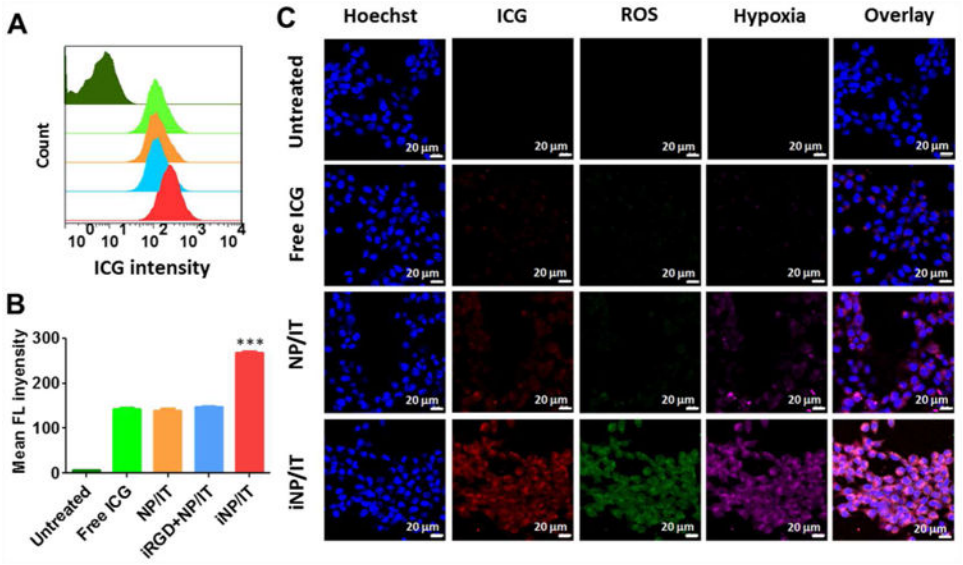

Figure 2.

Cell uptake and ability of the nanoparticles to generate intracellular ROS and hypoxia in 4T1 cells. (A) Cell uptake analyzed by flow cytometry. Top-to-bottom: untreated cells, cells treated with free ICG, NP/I, iRGD+NP/IT and iNP/IT after 6 h incubation. (B) Quantification of cellular uptake shown as mean fluorescence intensity/cell ± SD, n = 3. ***$p < 0.001$ vs. iRGD+NP/IT. (C) ROS and hypoxia generation following incubation of the cells with nanoparticles and laser irradiation. Confocal images of the cells stained with ROS and hypoxia probes. Cell nuclei were stained by Hoechst 33258, scale bar 20 μm.

Author Manuscript Author Manuscript Author Manuscript Author Manuscript

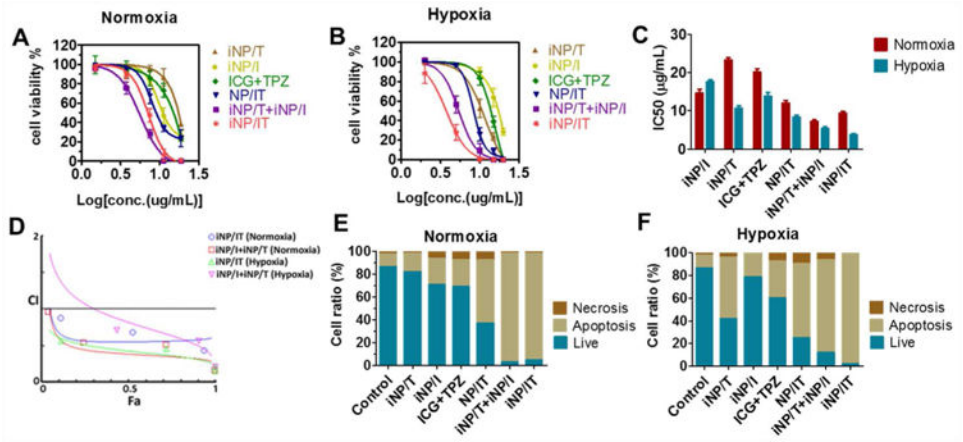

Figure 3.

Effect of nanoparticles on the cell viability and apoptosis in 4T1 cells. Cell viability of 4T1 cells following laser irradiation (except iNP/T) under (A) normoxia and (B) hypoxia for 24 h. (C) IC50 values in hypoxic and normoxic conditions (D) Analysis of the synergism. The corresponding CI vs Fa plots of iNP/IT and iNP/T+ iNP/I under different oxygen conditions. Flow cytometry analysis of 4T1 cell apoptosis induced by various formulations for 24 h using the Annexin V-FITC/PI staining under (E) normoxia and (F) hypoxia. Results shown as the means ± SD (n = 3).

Author Manuscript Author Manuscript Author Manuscript Author Manuscript

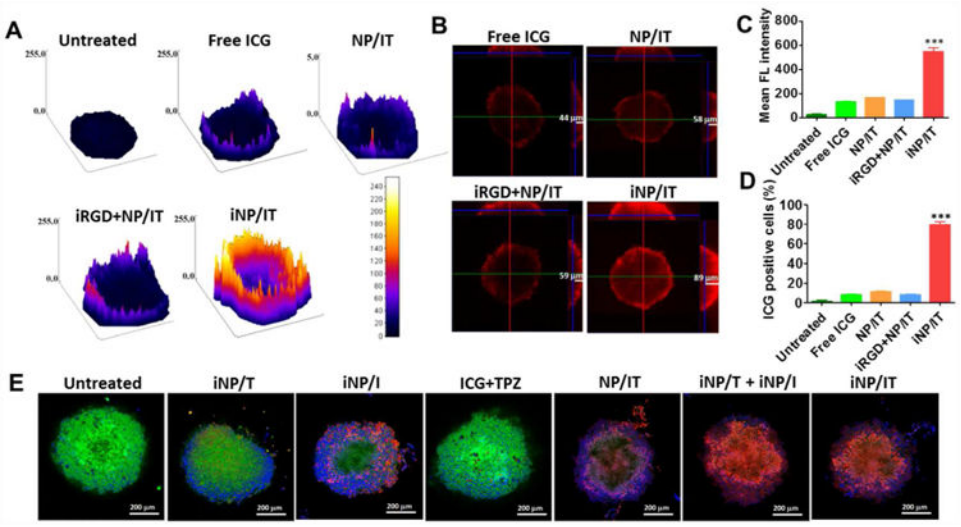

Figure 4.

Penetration and cell killing activity of the nanoparticles in 4T1 spheroids. (A) Surface plot images of 4T1 spheroids treated with free ICG, NP/IT, iRGD+NP/IT, iNP/IT and negative control. (B) Confocal microscopy images of spheroids after different treatments (X, Y and Z direction). (C) and (D) Accumulation of ICG in 4T1 cells from spheroids as indicated with mean fluorescence intensity and positive cell percent after flow cytometry analysis. Results are shown as mean ± SD, n = 3. ***$p < 0.001$ vs. iRGD+NP/IT. (E) Representative confocal images of live/dead viability assay in 4T1 spheroids treated with different formulations for 24 h (w or w/o NIR irradiation). Live cells were stained with calcein AM (green), the dead cells were labeled with EthD-1 (red). Nucleus was stained with Hoechst 33258 (blue).

Author Manuscript Author Manuscript Author Manuscript Author Manuscript

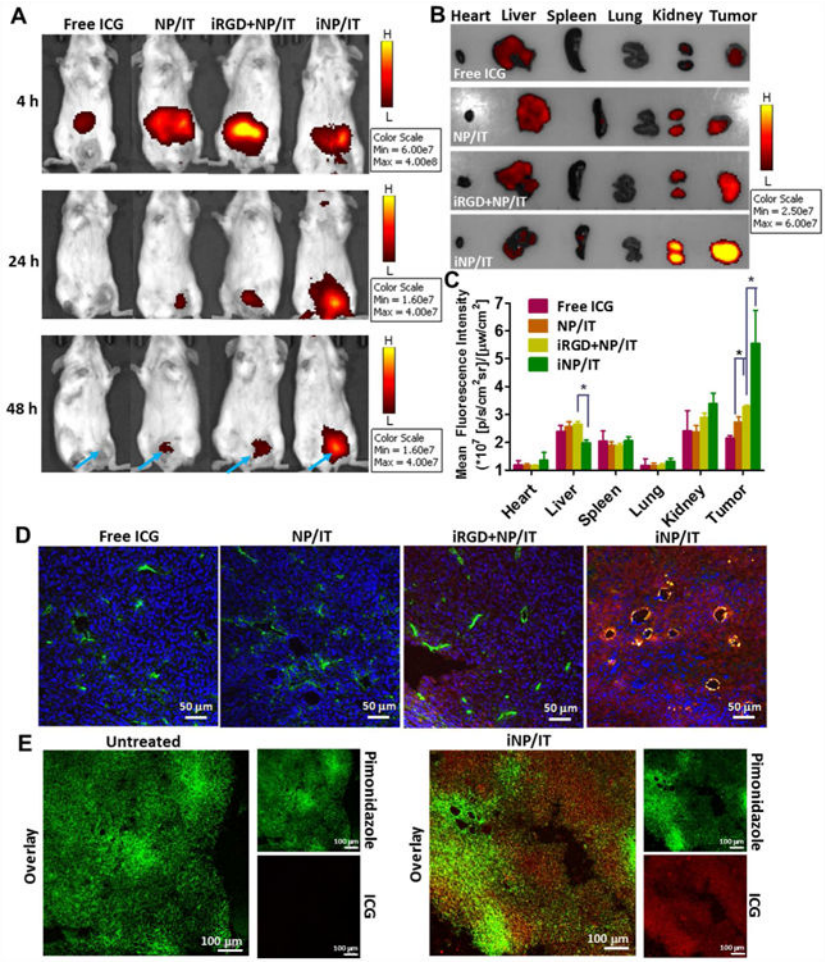

Figure 5.

Improved tumor delivery and penetration of nanoparticles *in vivo* in 4T1 orthotopic tumor-bearing mice. (A) *In vivo* imaging of mice at 4, 24, and 48 h after intravenous injection of free ICG and different nanoparticles. (B) *Ex vivo* images of tumors and other tissues at 48 h after injection. (C) Semi-quantification of nanoparticle biodistribution in mice tissues collected at 48 h post-injection. Results are expressed as mean fluorescence intensity ± SD (n = 3). *$p < 0.05$. (D) Confocal images of frozen tumor sections. Tumor blood vessels were labeled with FITC-CD31 antibody (green). ICG is shown in red and nucleic in blue (Hoechst 33258). (E) Hypoxia visualization in 4T1 tumors. Representative confocal images of frozen tumor sections stained with pimonidazole antibody (green).

Author Manuscript Author Manuscript Author Manuscript Author Manuscript

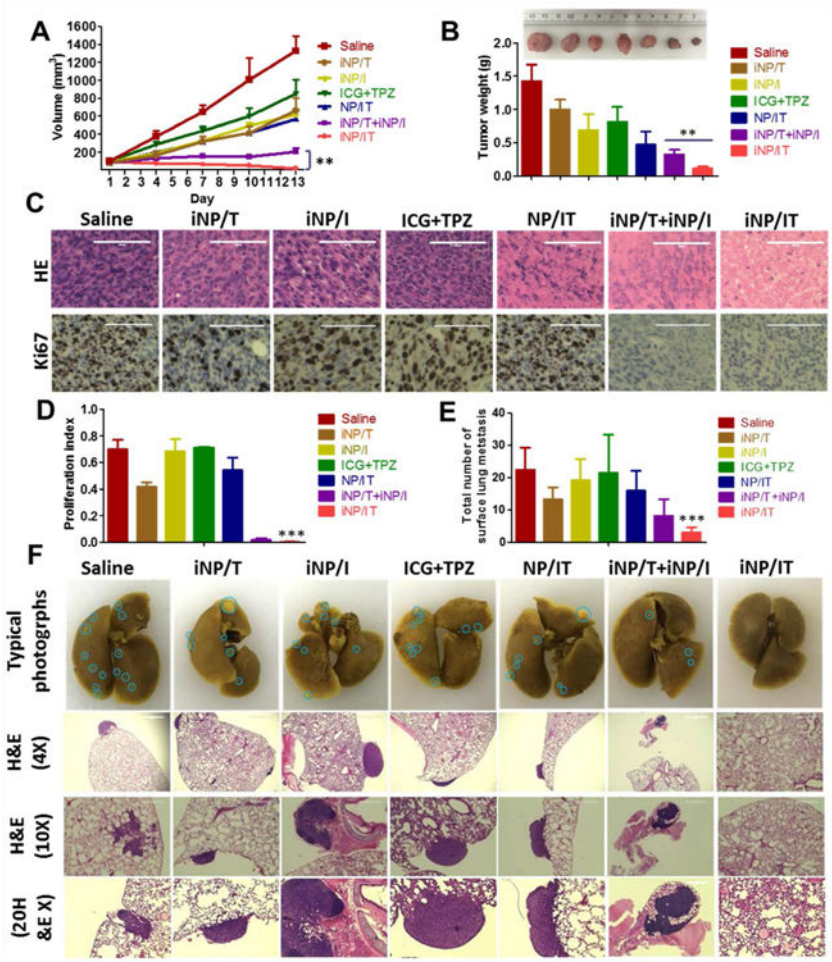

Figure 6.

Therapeutic efficacy and antimetastatic activity in metastatic 4T1 orthotopic tumor model. (A) Tumor growth profiles in mice treated with saline, iNP/T, iNP/I, free ICG+TPZ, NP/IT, iNP/T+iNP/I, and iNP/IT w or w/o laser irradiation. (B) Representative images and weight of collected tumors. Results are expressed as mean ± SD (n = 5). $^{**}p < 0.01$. (C) Histological analysis of tumor sections stained with H&E and Ki-67. Scale bars are 100 μm. (D) The corresponding proliferating index in the tumor tissue in Ki-67 staining assay. Data are expressed as mean ± SD (n = 3). $^{***}p < 0.001$ vs. control. (E) Average number of surface lung metastases. Results shown as average number of metastases observed under dissecting microscope ± SD (n = 5). $^{***}p < 0.001$, vs. untreated control. (F) Representative photographs of the whole lungs from mice treated with different formulations and H&E staining of the lung tissue sections (4×, 10× and 20×). Blue circles denote surface lung metastases.

Author Manuscript Author Manuscript Author Manuscript Author Manuscript

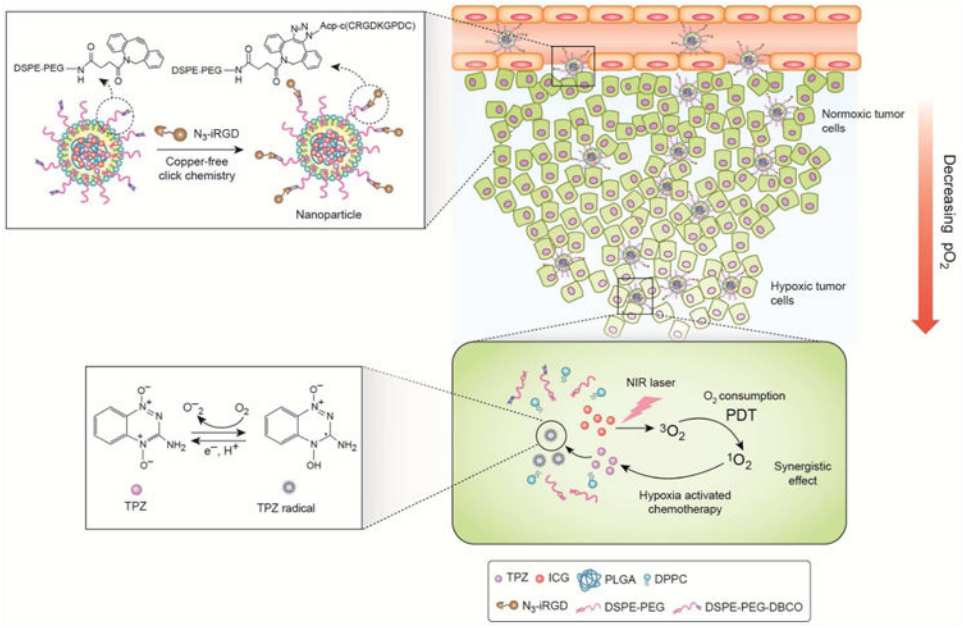

Scheme 1.

Mechanism of action of tumor-penetrating nanoparticles in combined PDT and hypoxia-activated treatment strategy.

Author Manuscript

Author Manuscript

Author Manuscript

Author Manuscript

Table 1

Sample identification

Sample	Description
ICG+TPZ	Mixture of free ICG and TPZ
NP/IT	NP loaded with ICG and TPZ
iRGD+NP/IT	Mixture of free iRGD peptide and NP loaded with ICG and TPZ
iNP/IT	iRGD-conjugated NP loaded with ICG and TPZ
iNP/I	iRGD-conjugated NP loaded with ICG
iNP/T	iRGD-conjugated NP loaded with TPZ
iNP/T+ iNP/I	Mixture of iRGD-conjugated NP loaded with ICG and iRGD-conjugated NP loaded with TPZ